

Full length article

Shape-preserving machining produces gradient nanolaminate medium entropy alloys with high strain hardening capability[☆]

Wei Guo^{a, e, *}, Zongrui Pei^b, Xiahao Sang^a, Jonathan D. Poplawsky^a, Stefanie Bruschi^c, Jun Qu^b, Dierk Raabe^d, Hongbin Bei^{b, f, **}

^a Center for Nanophase Materials Sciences, Oak Ridge National Laboratory, Oak Ridge, TN, 37831, USA

^b Materials Science and Technology Division, Oak Ridge National Laboratory, Oak Ridge, TN, 37831, USA

^c Department of Industrial Engineering, University of Padova, Padova, 35131, Italy

^d Department of Microstructure Physics and Alloy Design, Max-Planck-Institut für Eisenforschung GmbH, Düsseldorf, 40237, Germany

^e Material Science Research and Development, Timken World Headquarters, North Canton, OH, 44720, USA

^f School of Materials Science and Engineering, Zhejiang University, Hangzhou, 310058, PR China

ARTICLE INFO

Article history:

Received 8 December 2018

Received in revised form

5 March 2019

Accepted 19 March 2019

Available online 22 March 2019

Keywords:

Medium entropy alloys

Transmission electron microscopy

Cryogenic hard turning

Nanolaminates

Phase transformations

ABSTRACT

A high density of grain boundaries can potentially increase structural materials' strength, but at the expense of losing the materials' strain hardening ability at high flow stress levels. However, endowing materials with grain size gradients and a high density of internal interfaces can simultaneously increase the strength and strain hardening ability. This applies particularly for through-thickness gradients of nanoscale interface structures. Here we apply a machining method that produces metals with nanoscale interface gradients. Conventional bulk plastic deformation such as rolling, a process applied annually to about 2 billion tons of material, aims to reduce the metal thickness. We have modified this process by introducing severe strain path changes, realized by leading the sheet through a U-turn while preserving its shape, an approach known as 'hard turning'. We applied this process at both room temperature and 77 K to a NiCrCo medium entropy alloy. Micropillar compression was conducted to evaluate the mechanical response. After hard turning at room temperature, the surface microstructure obtained a ~50% increase in yield stress (0.9 GPa) over the original state with homogeneous grain size (0.4 GPa), but the initial strain hardening rate did not show significant improvement. However, after hard turning at 77 K, the gradient nanolaminate structure tripled in yield stress and more than doubled its initial strain hardening rate. The improvements were achieved by introducing a specific microstructure that consists of gradient nanolaminates in the form of nanospaced twins and martensite in the face center cubic (fcc) phase. This microstructure was formed only at cryogenic temperature. It was found after turning at room temperature that only nanospaced twins were present in the fcc phase inside nanolaminates that had formed at the surface. The origin of the enhanced strain hardening mechanism was studied. Joint density functional theory (DFT) and axial next nearest neighbor Ising (ANNNI) models were used to explain the temperature-dependent phase formation of the NiCrCo nanolaminate at the surface of the hard-turned material.

© 2019 Acta Materialia Inc. Published by Elsevier Ltd. All rights reserved.

1. Introduction

Structural materials can be strengthened by introducing high

densities of internal interfaces such as grain boundaries (GB) and twin boundaries (TB). However, interfaces introduce both desirable and undesirable properties. For example, compared to samples

[☆] This manuscript has been authored by UT-Battelle, LLC under Contract No. DE-AC05-00OR22725 with the U.S. Department of Energy. The United States Government retains and the publisher, by accepting the article for publication, acknowledges that the United States Government retains a non-exclusive, paid-up, irrevocable, world-wide license to publish or reproduce the published form of this manuscript, or allow others to do so, for United States Government purposes. The Department of Energy will provide public access to these results of federally sponsored research in accordance with the DOE Public Access Plan (<http://energy.gov/downloads/doe-public-access-plan>).

^{*} Corresponding author. Center for Nanophase Materials Sciences, Oak Ridge National Laboratory, Oak Ridge, TN, 37831, USA.

^{**} Corresponding author. Materials Science and Technology Division, Oak Ridge National Laboratory, Oak Ridge, TN, 37831, USA

E-mail addresses: wguo2007@gmail.com (W. Guo), hbei2018@zju.edu.cn (H. Bei).

with micron-sized grains (200 MPa), homogeneous nanocrystalline copper exhibits high strength above 650 MPa but at the cost of reduced tensile ductility [1]. One major challenge, therefore, is to increase the materials' strain hardening capabilities at high-stress levels in order to achieve a desirable mechanical response under loading scenarios that require the synergy of high strength and formability.

Developing materials with interface density gradients is a successful design strategy in nature as demonstrated by bamboo [2], squid beaks [3], human bones [4], lobster carapaces [5] and crab claws [6]. In these materials, the density of the internal interfaces varies from the surface to the interior. Inspired by nature, the synthesis and study of artificial gradient nanostructures have gained considerable interest in disciplines as diverse as tribology [7], biomechanics [8], fracture mechanics [9] and nanotechnology [10] where significant property improvement has been achieved through such structures. For instance, the strength-ductility dilemma experienced in nanocrystalline materials was reconciled by employing a heterogeneous grain structure, with increasing grain sizes from the surface to the inner part of the sample. The smaller grains at the surface deform less while the larger interior grains deform plastically – allowing both bulk strength and ductility to be simultaneously improved [11–15].

Corresponding synthesis and processing strategies for such materials include surface mechanical attrition (SMAT) [13,16–18], surface mechanical grinding (SMGT) [1], and thermo-mechanical methods [15,19]. Among these approaches, hard turning is a well-established method in the bearing steel industry that can be applied to machine steels to obtain a surface hardness above 45 Rockwell hardness (~ 4.4 GPa in nanohardness) [20]. With this method, alloys are high-throughput machined into the desired shape while acquiring a nanocrystalline surface layer conveyed from severe plastic near-surface shear deformation. Machining parameters such as turning speed and temperature can be readily modified to obtain desirable interface and substructure gradients [21,22]. These features establish hard turning as a simple and high-throughput surface-modifying manufacturing method, capable of processing larger quantities of bulk material.

In this study, we hard turn a NiCrCo medium entropy alloy (MEA) to render its microstructure interface-graded. We selected this alloy because to date, NiCrCo has exhibited the best combination of cryogenic strength (1.3 GPa), ductility (90%), and fracture toughness ($275 \text{ MPa m}^{1/2}$) among a wider family of transition metal element-composed, equiatomic alloys such as NiFe, NiCo, NiCrCo, and CrMnFeCoNi [23,24]. The outstanding cryogenic mechanical properties of NiCrCo alloy have been partially attributed to deformation-induced nanotwinning as a result of its low stacking fault energy (SFE) of $<5 \text{ mJ/m}^2$ compared to pure Ni ($>120 \text{ mJ/m}^2$) [25]. After cryogenic hard turning of the material, we observe a nanolaminate gradient structure consisting of densely populated nanotwin layers and hcp lamella inside the nanoscaled grains. We observe that the structurally graded alloy after 77 K hard turning exhibits high yield stress (1.4 GPa) and a high strain hardening rate (13.3) at 2% initial strain, a value 200% above those of established materials. Atom probe tomography (APT), transmission electron microscopy (TEM), and mechanical property measurements are used to study the gradient nanostructure and the material's temperature-dependent martensitic phase transformation response.

2. Materials and methods

2.1. Materials preparation

The NiCoCr MEA was produced from high-purity elemental

metals ($>99.9 \text{ wt\%}$), using arc-melting in an argon atmosphere. To ensure good elemental mixing, the melted button was flipped and remelted at least five times before drop-casting into rectangular cross-section copper molds measuring $25.4 \times 19.1 \times 127 \text{ mm}^3$. The ingots were then homogenized at 1200°C for 24 h in the vacuum and cold-rolled at room temperature (RT) along the 25.4 mm side to a final thickness of about 10 mm. The rolled bars were subsequently annealed at 900°C for 1 h in the air, producing bars with a fully recrystallized microstructure and an average grain size of $\sim 15 \mu\text{m}$ in diameter. The 10 mm rod-shape specimens were machined for further processing. The surfaces of the samples were hard turned at a speed of 40 m/min, which is equivalent to a strain rate of 10^4 – 10^5 s^{-1} within the top $10 \mu\text{m}$ of the surface. The hard turning was conducted at both 77 K and RT.

2.2. Materials characterization

An FEI Nova 200 NanoLab dual-beam focused ion beam (FIB) instrument was used to perform site-specific lift-outs of specimen regions of interest (ROIs), and the needle-shaped APT specimens were fabricated by annular milling. A wedge lift-out geometry was used to mount multiple samples on a Si microtip array to enable the fabrication of multiple APT needles from one wedge lift-out [26,27]. APT was performed with a CAMECA LEAP 4000X HR. During the data collection process, atoms from the surface of a cryogenically cooled needle-shaped specimen were field evaporated in an atom-by-atom fashion. The measurements were performed in laser mode with a 50 pJ pulse energy at 30 K and a detection rate of 0.005 atoms per pulse. The collected dataset was reconstructed using CAMECA IVAS 3.6.12 software.

Cross-sectional TEM samples close to the hard turned surface were FIB-prepared by using the FEI Nova 200 dual-beam focused ion beam (FIB). The TEM lamellas were ion milled by a 30-kV Ga ion beam and finally polished at 5 kV. After reaching a thickness of $\sim 100 \text{ nm}$, a Fischione Model 1040 NanoMill[®] was used to further clean the FIB damaged surfaces following the sequence of 1500 eV for 30 min and 900 eV for 10 min using an Ar ion beam with a 190 μA current. Selected area diffraction (SAD) and bright field TEM were acquired using a Hitachi HF3300 TEM operated at 300 kV, while high resolution scanning transmission electron microscopy (STEM) images were acquired using a probe corrected Nion Ultra-STEM 100 operated at 100 kV.

2.3. Mechanical testing

The hardness and indentation moduli of the materials were measured with a nanoindenter XP-MTS with a diamond Berkovich indenter tip. Tests were conducted to a prescribed maximum load $P = 20 \text{ mN}$ in a continuous stiffness mode (CSM) [28] at a constant loading rate of $(dP/dt)/P = 0.05 \text{ s}^{-1}$. A minimum of 20 nano-indentations was conducted on areas of the specimen to obtain averages and standard deviations for hardness and Young's modulus.

To obtain the stress and strain response in the different layers of the materials, pillars with an initial diameter of $\sim 2 \mu\text{m}$ were fabricated using a top-down milling method, starting at the top surface of the machined layer. The FEI Nova 200 dual-beam FIB system was operated at a final beam current of 86 pA and a constant accelerating voltage of 30 kV. A detailed description of the top-down milling method can be found in previous work [29]. The normal plane of the micropillars was determined by electron backscatter diffraction (EBSD). The pillars were inside a $40 \mu\text{m}$ diameter crater, leaving enough space for a $15 \mu\text{m}$ flat punch tip to avoid simultaneous contact with the surrounding bulk while the pillar was contacted. The mechanical properties of the FIB-milled micropillars

were measured in compression using a NANO Indenter[®] XP equipped with a flat punch diamond tip. The experiments were run in load control mode at a constant loading rate of 0.1 mN/s to a prescribed maximum displacement of 400 nm. The displacement during the compression was recorded at a frequency of 10–20 Hz. The initial compressive stress, $\sigma = F/A_0$, was obtained from the measured load (F) at 0.2% offset force and the pillar cross-sectional area A_0 at 20% of its height away from the top of the pillar since the deformation was confined to the top due to the tapered geometry. The engineering strain was obtained by dividing the displacement over the pillar height.

Ball-on-flat reciprocating sliding tribological tests were conducted on a Plint TE-77 tribometer (Phoenix-Tribology Ltd.) using an MEA cylinder (8 mm diameter) against an M2 steel flat ($25.4 \times 25.4 \text{ mm}^2$ worn area and 3.175 mm thick). Tribological tests were performed at both cryogenic temperature and RT under a 10 N normal load with a 10 Hz oscillation and a 10 mm stroke for 50 m of sliding. At least three tests were performed for each sample. Friction force was captured in situ using a piezoelectric load cell. After testing, all specimens were cleaned with acetone followed by isopropyl alcohol. Wear volumes on the cylinders were then quantified using a Wyko NT9100 white light interferometer.

2.4. Theoretical calculations for nanophase stability

The Gibbs free energy of a system can be calculated by:

$$F(V, T) = E_{0K}(V) + F_{el}(V, T) + F_{vib}(V, T) + F_{mag}(V, T) - TS_{conf.}(T) \quad (1)$$

where $E_{0K}(V)$ is the total energy of the structure at 0 K, $F_{el}(V, T)$ is the electronic free energy, $F_{vib}(V, T)$ is the vibrational energy, $F_{mag}(V, T)$ is the magnetic energy, and $S_{conf.}(T)$ is the configurational entropy. Spin-polarized density functional theory (DFT) calculations are performed to calculate the total energy at 0 K $E_{0K}(V)$. In evaluating the Gibbs free energy $F(V, T)$, we neglect the magnetic contribution and the contribution from $S_{conf.}(T)$, as conducted by other researchers [30–32]. The electronic free energy $F_{el}(V, T)$ is calculated using the DFT-computed electronic density of states and the temperature is introduced by the Fermi-Dirac distribution. More details can be found in the work by Grabowski et al. [33].

There is a lack of feasible and practical methods to calculate the vibrational free energies of multicomponent alloys. Here, the Debye–Grüneisen model [34] was used to treat the vibrational part of the free energy, i.e.,

$$F_{vib}(V, T) = E_D(V, T) - TS_{vib}(V, T), \quad (2)$$

with $E_D(V, T)$ and $S_{vib}(V, T)$ given by

$$E_D(V, T) = \frac{9}{8}k_B\theta_D(V) + 3k_BTD(x), \quad (3)$$

$$S_{vib}(V, T) = 3k_B \left[\frac{4}{3}D(x) - \ln(1 - e^{-x}) \right], \quad (4)$$

where k_B is the Boltzmann constant, $x = \frac{\theta_D(V)}{T}$, and $D(x)$ is the Debye function.

The Debye temperature is calculated by

$$\theta_D(V) = 41.63 \sqrt{\frac{r_0 B_0}{M}} \left(\frac{V_0}{V} \right)^\gamma, \quad r_0 = \left(\frac{3V_0}{4\pi} \right)^{\frac{1}{3}}, \quad (5)$$

where 41.63 is an empirical constant, r_0 is the atomic radius, V_0 is the equilibrium volume, M is the atomic mass (atomic units), and B_0

is the bulk modulus. The Grüneisen parameter is defined by

$$\gamma = -g - \frac{\partial^2 P / \partial V^2}{\partial P / \partial V} = -g + \frac{1}{2} \left(1 + B'_0 \right), \quad (6)$$

Here, B'_0 is the bulk modulus pressure derivative, and g is a temperature-dependent factor. We use a value of $g = 2/3$ following [30]. The parameters involved in the equations are given in Table S2.

Spin-polarized DFT computations were performed for the total energies of the hcp, fcc and dhcp NiCoCr phases using the Vienna Ab-initio Simulation Package (VASP) [35,36]. The generalized gradient approximation (GGA) with Perdew–Burke–Ernzerhof parameterization [37] was employed to describe the exchange–correlation interaction. A plane-wave cutoff energy of 350 eV and gamma-based-scheme dense k-points \times atoms were used to ensure that the total energies converged to values around 1 meV/atom. More specifically, 5832, 4050 and 2700 k-points \times atoms were adopted for the fcc, hcp and dhcp (double hcp) supercells. Energies of the ionic step were converged within 10^{-4} eV. Supercells comprising 72 atoms for dhcp and 54 atoms for fcc and hcp structures were chosen to mimic the chemical randomness. A smaller supercell of 48 atoms demonstrated that the energy bands of the fcc and hcp structures overlap. Static calculations were performed for all three structures with eight times denser k-meshes. The electronic density of the states was sampled using 2201 points.

3. Results

3.1. Materials processing and nanostructure characterization

We synthesized a NiCrCo MEA alloy and subjected it to hard turning to imprint a nanostructure gradient. This process imposes severe shear deformation at a turning speed of 40 m/min, equivalent to a strain rate of $3.5\text{--}4.7 \times 10^4 \text{ s}^{-1}$ in the top 5 μm surface region of the material (see supplementary materials for a detailed calculation). The microstructure hierarchy is characterized by cross-sectional TEM and STEM. A cross-sectional bright-field image (Fig. 1b) reveals the resulting microstructure hierarchy from the surface to several μm into the material. Along the direction of the hard-turned surface (left), the microstructure exhibits strain-dependent features: a nanocrystalline zone was formed in a $\sim 2 \mu\text{m}$ near-surface layer (Fig. 1b and c), and a mixed deformed structure with a high density of dislocation cells and an nm-scale deformation twinning structure was formed below this region (Fig. 1b and f). The average grain size is about 0.278 μm in the topmost 50 μm (Fig. 1e) and the grain size is $102.8 \pm 46.3 \text{ nm}$ in the top 2 μm , whereas significant nanotwinning and dislocation cell structures are observed beneath the nanocrystalline layer. High angle annular dark field (HAADF)-STEM imaging of the interiors of the nanosized grains reveals two main features that contribute to the complex nanostructure hierarchy: the grains contain 0.9–4.8 nm sized twins and hcp structured regions of similar dimension. (Fig. 1g and h). The hcp laths assume a coherent orientation relationship with their respective fcc grains, with $(0001)_{\text{hcp}} // (111)_{\text{fcc}}$ and $[11\text{--}20]_{\text{hcp}} // [1\text{--}10]_{\text{fcc}}$, and the hcp laths share the $\{111\}$ habit planes as coherent boundaries of the nanotwins. The fcc lattice parameter, a_0 , was measured to be 0.3524 nm and the average hcp lattice parameters were measured to be 0.2349 nm and 0.3836 nm for a_0 and c_0 , respectively. A schematic of the layered image projected along the zone axis of $[110]_{\text{fcc}}$ is shown in Fig. 1i.

We also investigated whether the same hard-turning condition could induce similar microstructures at room temperature (RT). As shown in Fig. 2a, a gradient nanostructure was formed at the

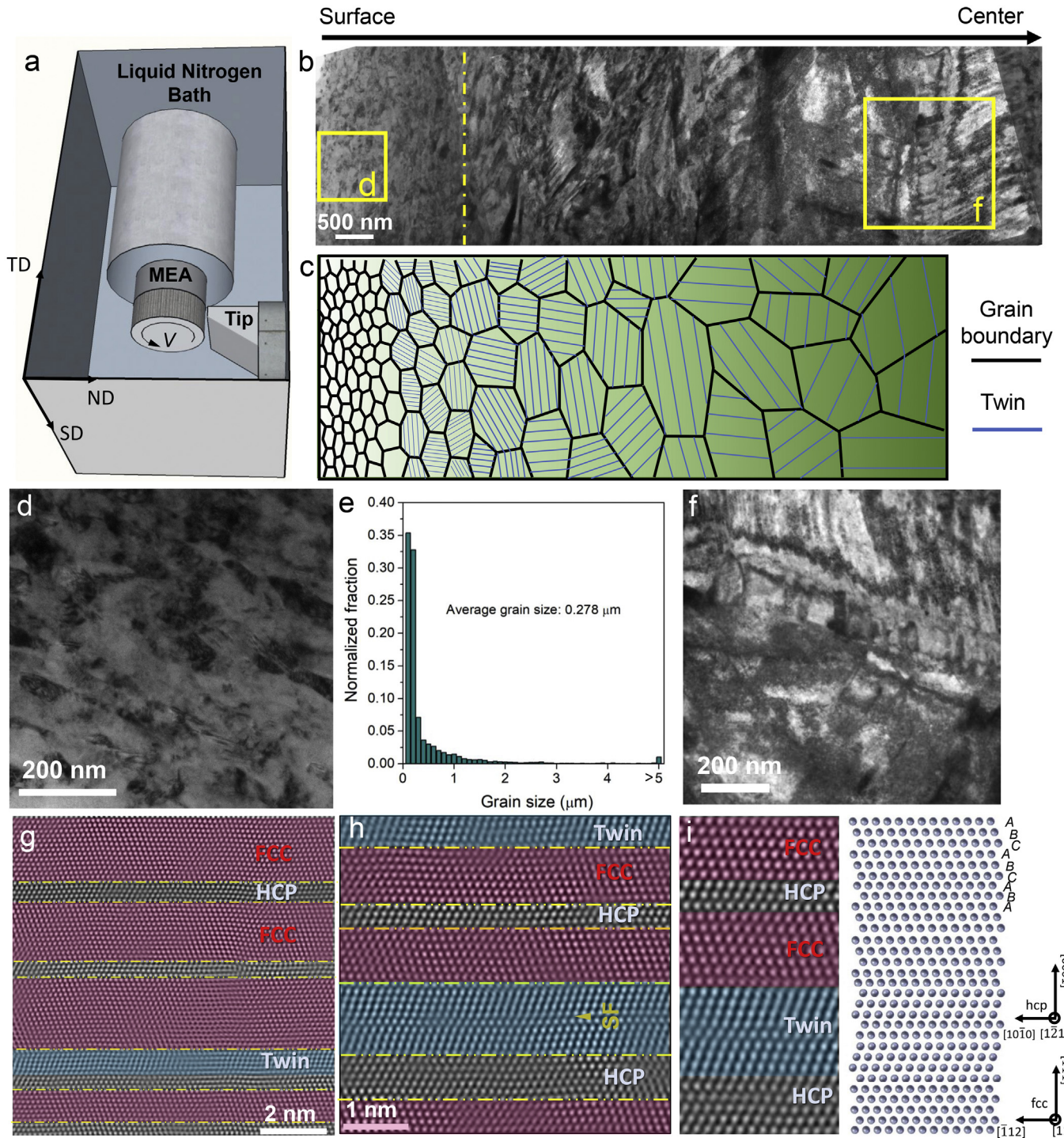


Fig. 1. Processing routine and microstructures of 77K hard-turn processed structure-gradient MEA. (a) Schematic of alloy processing procedure. (b) Cross-sectional bright-field (BF) TEM image revealing the gradient structure of the deformed surface region. (c) Schematic image showing the gradient nanostructure after cryogenic hard turning. (d) BF-TEM showing nanograin structure. (e) Grain size distribution in the topmost 50 μm surface layer of the material. (f) BF-TEM showing a coarser grain structure in the subsequent layer. (g,h) Atomic resolution HAADF STEM images showing structural hierarchy inside single nanocrystalline grains along the $[110]_{\text{fcc}}$ zone axis. The image has been enhanced using a Bragg filter. The fcc phase, hcp lamella, and nanotwins are highlighted by pink, black, and blue colors, respectively. Yellow dashed lines mark boundaries between different phases. (i) Schematic of atom stacking of nanolaminate along the $[110]_{\text{fcc}}$ zone axis within a single nanograin. (For interpretation of the references to color in this figure legend, the reader is referred to the Web version of this article.)

surface when processed at RT, but the thickness of the retained nanocrystalline layer was below 1 μm , i.e., much thinner than that formed at the cryogenic temperature ($\sim 4 \mu\text{m}$). The average grain size in the topmost 50 μm of the material close to the surface is about 1.00 μm (Fig. 2c). On-zone STEM imaging was performed on

the deformed substructures (Fig. 2d and f). Similarly, a nanoscale laminate substructure was formed, consisting of fcc/twin zone bundles, with the twin thicknesses ranging from 0.9 nm to 7.8 nm and the twin spacing between 1.2 nm and 15.9 nm. The twin boundaries contain step-type defects due to dislocation

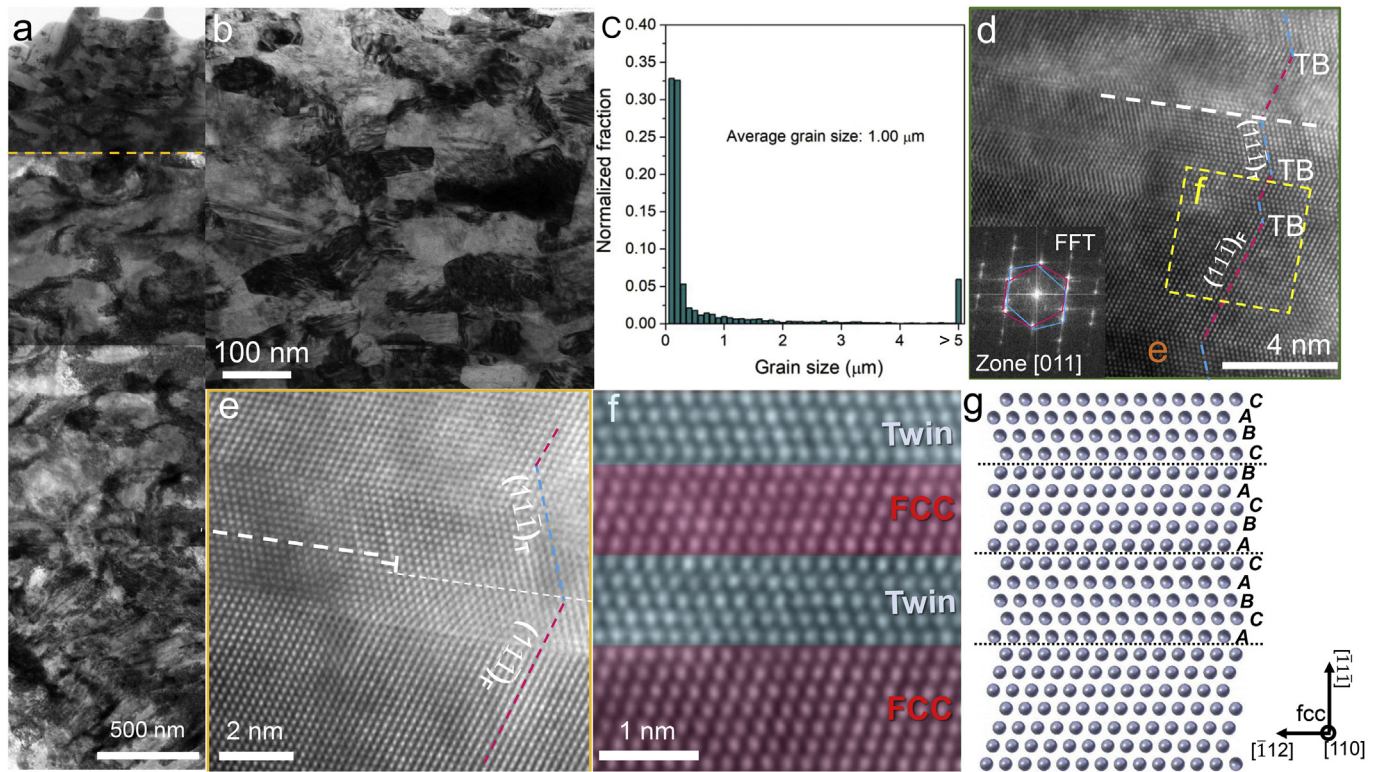


Fig. 2. Gradient microstructure of medium entropy alloys produced by hard turning at room temperature. (a) Cross-sectional BF-TEM image showing gradient structure of deformed surface; (b) BF-TEM image of nanocrystalline grain layer; (c) Grain size distribution in the topmost 50 μm surface layer of the material; (d) STEM images showing high density of nanotwins inside single grain; (e, f) BF-TEM images of nanotwins indicate that most of fcc/twin interfaces are coherent, with Shockley partial dislocations located at the TBs; (g) Schematics showing nanolaminate stack structure in nanocrystalline layer.

intersections.

In materials with low SFE, a perfect dislocation dissociates into two Shockley partial dislocations. The incoming leading partial dislocations react with the twins while the trailing ones get stored at the TB (see Fig. 2e). The interaction of twins and dislocations increases the strength and ductility of the materials [38,39]. hcp phase formation was not observed when processed at RT. A schematic of the layered image projected along the zone axis of $[110]_{\text{fcc}}$ is shown in Fig. 2g.

The APT analysis was carried out on tips extracted from the hard-turned surface at cryogenic temperature to probe the chemical homogeneity at the TBs. Grain boundaries and planar features are revealed due to the local magnification effect [40] (shown in Fig. 3). For clarity, the GBs are marked with dashed lines in Fig. 3. Frequency distribution analysis reveals that the three alloying elements in the cryo-processed material are distributed homogeneously, indicating an athermal fcc-to-hcp phase transformation mechanism as observed in Fig. 1. Also, three planar linear features are shown in Fig. 3c, which are most likely nanotwin boundaries. One dimensional concentration analysis along the twinning structures shows that there is no obvious chemical segregation to the TBs (Fig. 3d).

3.2. Mechanical testing of the medium entropy alloy nanolaminates

Nanoindentation experiments were performed to evaluate the effects of the observed structural changes on the mechanical properties. More than 20 nanoindenters were performed at the surfaces after hard turning and also within the base material to avoid the influence of any local structural inhomogeneities. Fig. 4 shows the load-displacement curves from the nanoindentation tests. The

surface obtained from hard turning at 77 K shows the largest nanoindentation hardness (5.63 ± 0.24 GPa). The surface hardness of the materials fabricated by hard turning at 300 K is slightly lower (5.47 ± 0.35 GPa) and that of the corresponding base materials is the lowest (4.90 ± 0.32 GPa). The measured reduced modulus E^* in Table 1 combines Young's modulus of the diamond indenter and the MEAs under different condition and is given by $\frac{1}{E^*} = \frac{(1-\nu^2)}{E} + \frac{(1-\nu'^2)}{E'}$, Where E and E' are the Young's modulus for the diamond indenter (1220 GPa) [41] and the material, and ν and ν' are the Poisson's ratios of the diamond indenter (~ 0.2) and of the MEAs (0.3) [23]. Based on this estimation, the Young's modulus for the baseline material for the cryogenic turned layer, and for the turned layer at room temperature are 261 GPa, 245 GPa, and 234 GPa, respectively. The reduction of Young's modulus after hard turning is primarily due to the grain size reduction from micron scale to nanometer scale, which agrees with earlier measurements which revealed that the apparent Young's modulus for various nanocrystalline materials such as iron and copper is substantially lower than that probed for conventional polycrystals [42].

Uniaxial micro-compression testing was conducted for samples obtained by the different processing conditions to determine differences in the load responses at the μm length scale. The pillars were fabricated from the surfaces of the unprocessed base material (reference) and from the surfaces of samples after hard turning at 300 K and 77 K (shown in Fig. 5 (a)-(c), respectively). For each sample condition, at least three pillars were tested to ensure the reproducibility. The pillars were prepared by focused ion beam milling to an approximate 2 μm top diameter and a 3° taper angle. After straining, the pillar prepared from the homogeneous MEA exhibited yield stress ($\sigma_{0.2}$) of 0.4 GPa and initial flow stress of

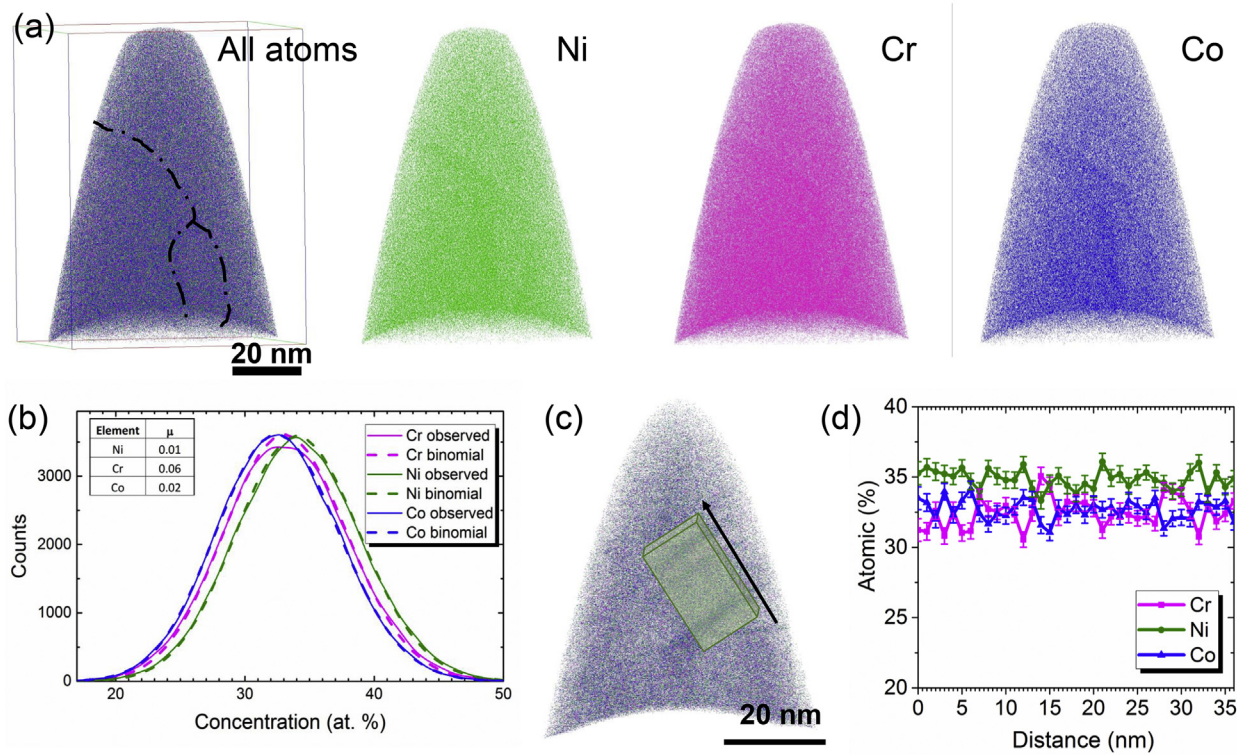


Fig. 3. APT analysis of nanocrystalline surface for MEA sample after cryo-hard turning. (a) APT elemental map of Ni, Cr and Co atoms; (b) Frequency distribution analysis for constituent elements, the binomial distribution for average solute elements are also for comparison, which represents an ideal homogenized alloy; (c) 3 nm slices of APT volumes showing the nanotwinning structure; (d) One-dimension concentration analysis of the region of interest indicated in c.

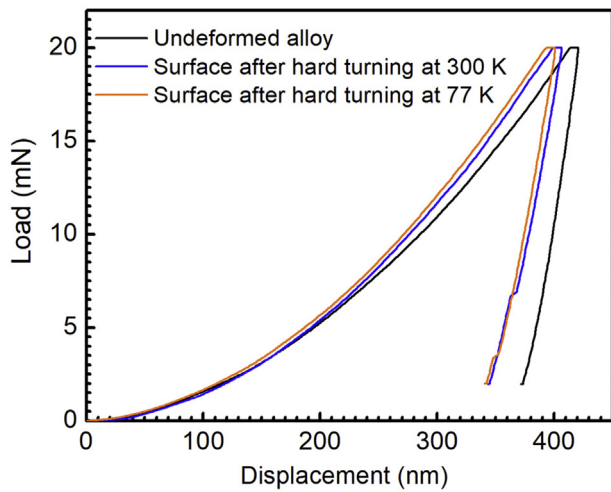


Fig. 4. Representative load-displacement curves from nanoindentation tests of NiCrCo MEA nanolaminates after different processing methods. The obtained nanohardness and residual modulus are averaged from 20 nanoindentation tests for each sample.

Table 1

Nanohardness and residual modulus are averaged from 20 nanoindentation tests for each sample.

	Baseline material	Cryogenic turned layer	RT turned layer
Nanohardness (GPa)	4.90 ± 0.32	5.63 ± 0.24	5.47 ± 0.35
Reduced modulus (GPa)	234 ± 9	222 ± 13	214 ± 11
Estimated Young's modulus (GPa)	261	245	234

1.1 GPa at 8% strain. The post-deformed pillar showed a series of parallel slip traces, indicating a dislocation-mediated deformation process (Fig. 5a). For the MEA hard turned at 300 K, the bottom of the tapered pillar (~1 μm from the surface) was much more deformed than the surface layer, i.e. the bottom region carried most of the initial strain (Fig. 5b). This can be explained by nanocrystallization and nanotwinning-induced strengthening of the layers, as documented in Fig. 2. The pillar prepared at the surface of the machined layer at 300 K has MEA exhibited yield stress ($\sigma_{0.2}$) of 0.9 GPa and initial flow stress of 1.6 GPa at 8% strain.

The pillar prepared at the surface of the machined layer at 77 K exhibited yield stress of 1.3 GPa and initial flow stress of 2.2 GPa at 8% strain, indicating that these pillars are much stronger than the pillars prepared from the homogeneous MEA (1.36 μm in average grain size) and surface layer hard turned at 300 K. Multiple slip traces from different directions can be observed from the images of the post-test pillars (Fig. 5c). Fig. 5e displays the strain hardening rate as a function of the plastic strain and compares the work-hardening ability among these three systems. The strain-hardening rate (Θ) was normalized by $\Theta = \frac{1}{\sigma_f} \frac{\partial \sigma_f}{\partial \epsilon}$, where σ_f represents the flow stress and ϵ is the true strain. It can be seen that Θ

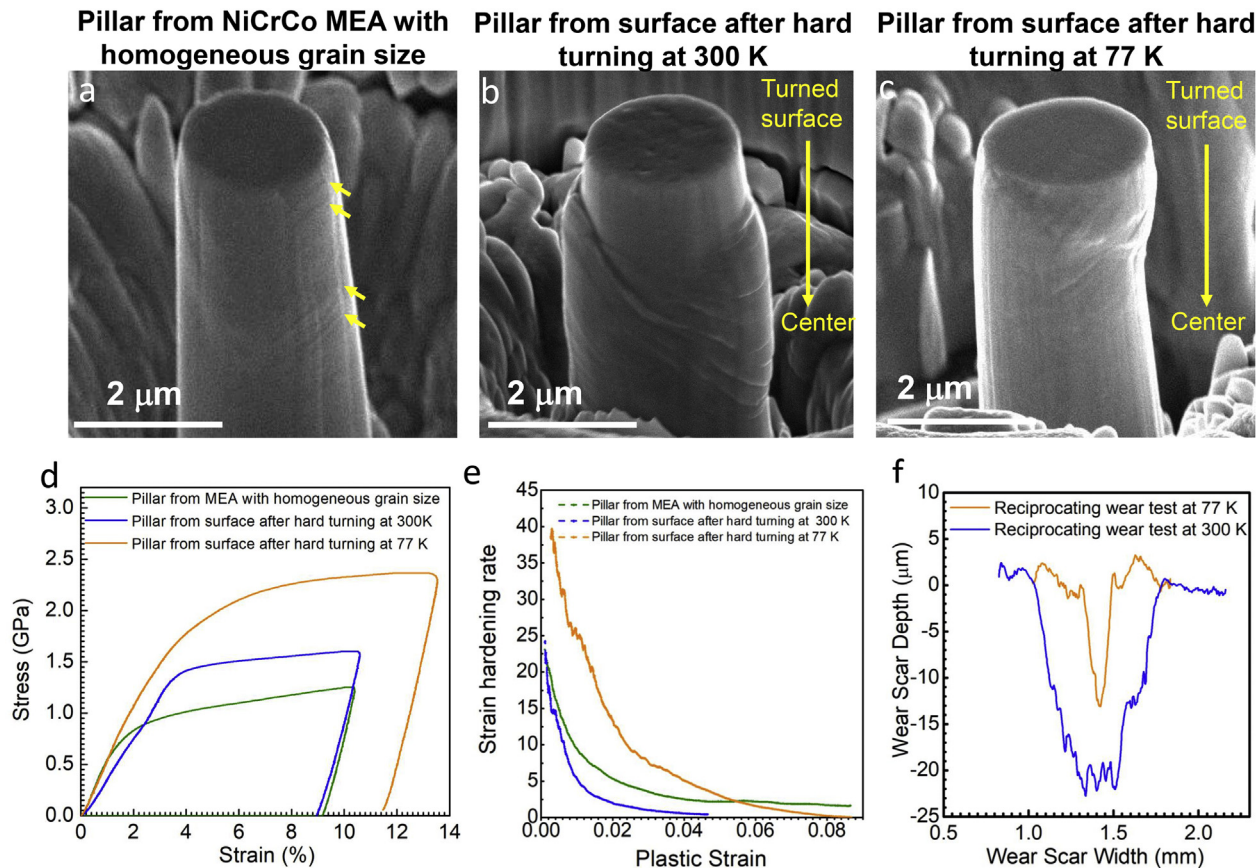


Fig. 5. Micropillar compression and reciprocating sliding wear tests of MEAs obtained under different processing conditions. (a–c) Surface morphologies of micropillars after micro-compression test (yellow arrows mark slip traces). (d) Engineering stress-strain curves of micropillar compression. (e) Strain-hardening rate vs. plastic strain; (f) Wear depth of the MEA surface after cylinder-on-flat reciprocating sliding wear test at 300 K and at 70 K. (For interpretation of the references to color in this figure legend, the reader is referred to the Web version of this article.)

decreases rapidly with increasing initial strain for the homogeneous MEA and RT turned MEA; however, the 77 K deformed surface material shows a more sluggish decrease in strain hardening rate. At 2% strain, the work-hardening rate for the 77 K pillar is 13.3, whereas the rate is 4 for pillars prepared from the surface after 300 K hard turning and 5 for the homogeneous MEA pillar.

The loading condition in a reciprocating sliding wear test is similar to that of the hard-turning process, in which severe shear deformation is imposed on the sample surface. Therefore, 8 mm diameter, 12 mm long MEA cylinders were used to test the wear behavior at different temperatures. Fig. 3f displays the wear depth of the MEA cylinder surface after the cylinder-on-flat reciprocating sliding wear test. Under the cryogenic condition, the maximum wear depth was 12.5 μm and the wear volume was $0.67 \times 10^7 \mu\text{m}^3$. At RT, the maximum wear depth was 22 μm with a wear volume of $4.42 \times 10^7 \mu\text{m}^3$. These results show that the wear resistance of the NiCrCo MEA processed at 77 K is much better than that produced at 300 K. In other words, the more enhanced gradient nanostructured surface (GNS) layer exhibits enhanced wear-resistance performance, which is analogous to enhanced wear resistance found in GNS layer of Cu alloys [43] and interstitial free steel [44].

4. Discussion

4.1. Formation of gradient nanolaminate medium entropy alloys

The strain gradient structure fabricated by hard turning not only

produces a grain-sized gradient from the machined surface to the center, but also demonstrates a phase hierarchy structure containing martensite, twinning, and fcc in each of the nanograins. First, decreasing the processing temperature can yield a more intense gradient structure, as evidenced by a thicker ($\sim 2.5 \mu\text{m}$) nanocrystalline layer formed at the subsurface (Figs. 1 and 2) compared to the more coarsely structured inner region of the material. A similar finding of grain size refinement during tensile testing of a NiCrCo alloy was reported by Yang et al. [45]. The authors showed that a microstructure starting with 4 grains/ μm^2 was refined to 21 grains/ μm^2 at room temperature and to 31 grains/ μm^2 at 77 K. The corresponding area fraction of the nanocrystals increased from 2.0% to 5.5% (deformation at room temperature) and 8.0% (deformation at 77 K). Similarly, the high efficacy of more intense gradient structures formed after hard turning at 77 K is due to NiCrCo's lower stacking fault energy, which facilitates the formation of more corner and necklace twins that subsequently can evolve into new nanograins.

The strain gradient structures fabricated by hard turning at different temperature also induce specific substructures and deformation mechanisms. Fig. 6 shows the thickness (Fig. 6a) and spacing (Fig. 6b) of nanotwins in the nanocrystalline surface layers obtained for the different processing conditions used. The thicknesses of the deformation-induced nanotwins ranges from 0.9 nm to 7 nm, and does not vary substantially with respect to the depth from the surface and the processing temperature. However, the spacing of the nanotwins formed during hard turning at RT tends to

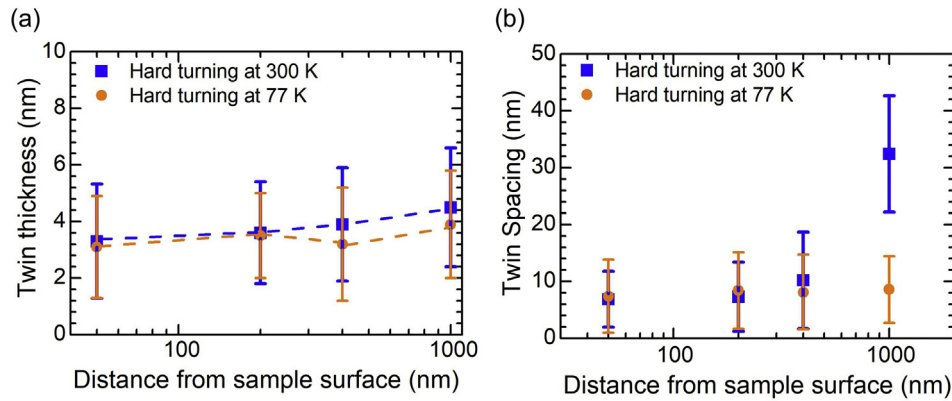


Fig. 6. Comparison of thickness (a) and spacing (b) of nanotwins for MEAs obtained by hard turning at different temperatures.

increase at ~1000 nm away from the surface where the effective plastic shear strain decreases along the sample depth direction. The spacing of the nanotwins created during hard turning at 77 K is below 10 nm on average, and this spacing does not change significantly with respect to the distance from the surface within the initial 1000 nm through the sheet thickness.

Previous work on NiCrCo subjected to different levels of deformation showed that the threshold strain for nanotwin formation in NiCoCr alloys is much higher at RT (~20%) than at cryogenic temperature (6.0%–8.8%) [46,47]. TEM analyses confirm that in the deeper layers (>1 μm below the surface) lower densities of nanotwins are formed at RT than at 77 K owing to the insufficient strain at such depths when exposed to RT processing (Fig. 6b).

4.2. Strain hardening mechanisms of gradient nanolaminate medium entropy alloys

The contribution of grain refinement to yield stress increase can be roughly estimated based on the average grain size before and after hard turning using the Hall-Petch relationship: $\Delta\sigma = K D_{\text{after}}^{-1/2} - K D_{\text{before}}^{-1/2}$, where $K = 500 \text{ MPa} \cdot \mu\text{m}^{1/2}$ is the coefficient of the Hall-Petch relationship for NiCrCo MEA [48]. Considering the average grain size measured in this study, the strain hardening due to grain size refinement can be estimated at about 41 MPa for the hard-turned surface at 300 K and 300 MPa for hard turned surface at 77 K. However, such strengthening is usually obtained at the expense of limited strain hardening, because the intragranular dislocation storage for nanograins is rather limited compared to the micron-sized materials. However, as shown in Fig. 5e, the hard-turned surface obtained at 77 K still shows appreciably more strain hardening ability than the homogeneous MEA, even at ~1.4 GPa flow stress levels. Next, we will discuss the strain hardening mechanism of gradient nanolaminate medium entropy alloys.

Fig. 7a shows the flow stress (minus yield stress $\sigma_{0.2}$) versus plastic strain at compression conditions for NiCrCo MEA with homogeneous grain size (~1.36 μm), the gradient NiCrCo nanolaminate MEA hard turned at 77 K and two austenitic stainless steels with micron sized grains [49,50]. The yield stresses in compression for the 304L and 416 austenitic stainless steel are ~200 MPa and ~550 MPa, respectively. As they are continuously loaded with 8% strain, a flow stress increase of less than 200 MPa can be observed. The NiCrCo MEA with homogeneous grain size shows a significant 650 MPa increase in flow stress when strained at 8%, this is mainly due to the deformation-induced twinning observed in the previous studies. Due to the material's very low SFE of <5 mJ/m² [25], the NiCrCo MEAs tend to form nanotwins during

deformation. Such deformation twins are only a few nanometers in thickness but provide effective barriers to dislocation motion and create nucleation and accommodation sites for dislocations, enhancing the alloy's ability to absorb plastic deformation energy [23,32,51]. In comparison, the gradient NiCrCo nanolaminate structured obtained after 77 K has a flow stress increase of over 900 MPa even when yielded with a very high stress level (1.1 GPa). Instead of following a monotonic drop, as did the homogeneous MEA and austenitic stainless steels, the initial strain-hardening rate for the NiCrCo nanolaminate decreases sluggishly in steps and is five times higher than the NiCrCo alloy with homogeneous grain size, when strained to 2%.

To further unveil the nanostructure origin of the high strain hardening, Fig. 8 shows the deformation structures of NiCrCo gradient nanolaminate after hard turning at 77 K. It is observed that numerous Shockley partial dislocations (short, white arrows) have been deposited at the twin boundaries (TBs). A large number of TBs provides locations where a high density of dislocations can move and be established from low levels. Most TBs observed in the cryogenic turned samples (Fig. 8a and b) lost their coherency as a result of the storage of Shockley partial dislocations. These partial dislocations not only create additional strain fields but also are mobile along the boundary plane (111), and are primary contributors to the plastic strain under the loading condition [52]. Frank partial dislocations (marked as T in Fig. 8) are also observed at both the grain interiors and TBs. These dislocations are sessile, contributing mainly to the strain hardening. In addition, considerable stacking faults (SFs) can be observed in the nanolayer lamella-shaped structures. Although the strain hardening from SFs is not as strong as from TBs as obstacles for dislocation moving [52], the SF/matrix boundaries can become additional storage sites for dislocations, as shown in Fig. 8.

The formation of hcp plates benefits from the formation of Shockley partial dislocations and SFs, which are known as precursors for hcp phase transformation in low stacking fault energy austenitic alloys [53]. The hcp/matrix phase boundaries around the (111)_{fcc} plane normal direction can become storage sites for Shockley partial dislocations, and their termination front can help lock down some immobile dislocations. Similarly, a partial fcc-to-hcp phase transition was observed in deformed Fe_{80-x}Mn_xCo₁₀Cr₁₀ (at.%) alloys [53], Co₂₀Cr₂₆Fe₂₀Mn₂₀Ni₁₄ HEAs [54], and NiCoCr alloys [47,48], where the hcp phase is only a few atomic layers thick. In many alloys, the hcp stacking is intrinsically stronger than the more ductile fcc structure, as in Mg [55,56] and in some hcp-based HEAs [57,58]. In the hcp phase only dislocations with out-of-basal-plane components (<c> or <c+a> dislocations) can accommodate the deformation along the closest-packed plane

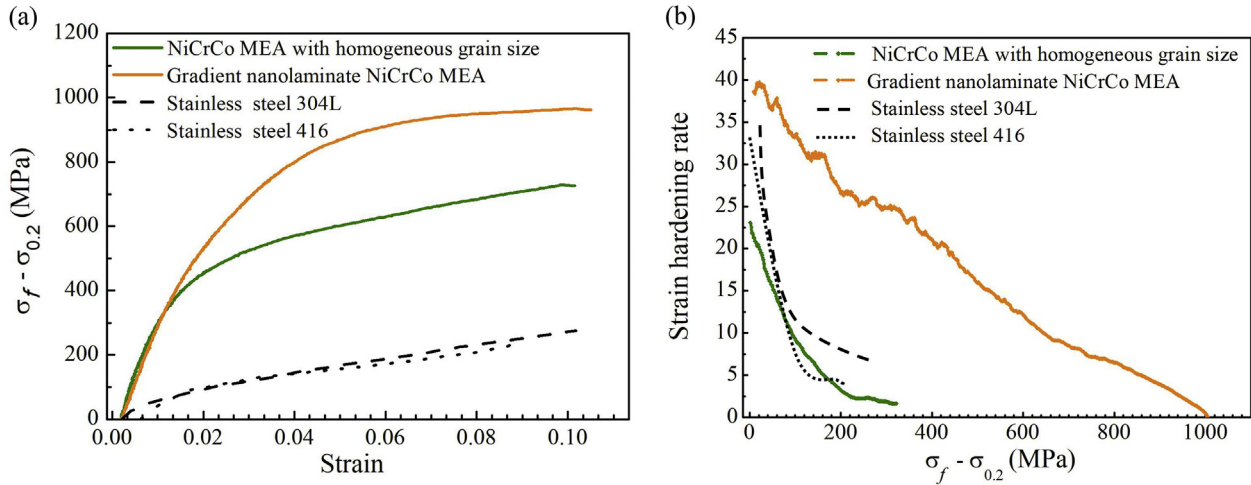


Fig. 7. (a). Reduced true stress (true stress minus yield stress) versus plastic strain curves; (b). Strain hardening rate as a function of reduced true stress. The gradient nanolaminate NiCrCo MEA fabricated after 77 K is compared with homogeneous NiCrCo MEA (1.36 μm in average grain size), as well as 304 L and 416 austenitic stainless steel with micron sized grains [49,50].

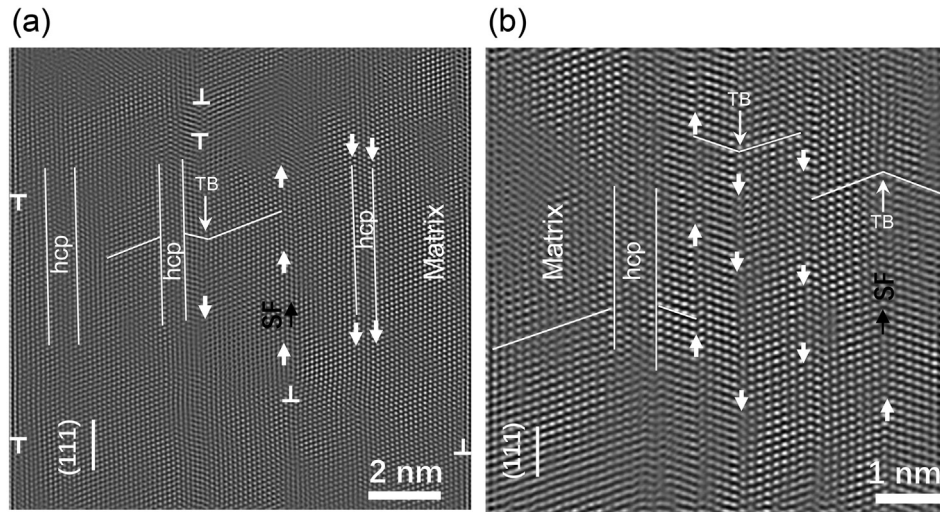


Fig. 8. High-resolution transmission electron micrographs (HRTEMs) showing the deposition of Shockley partial (short arrows) and Frank (T) partial dislocations at twin boundaries and at hcp/matrix interfaces, after cryogenic hard turning at 77 K. Dislocation interactions with twin boundaries, the hcp phase, and stacking faults are also marked in the figure.

normal. The activation of these dislocation types typically requires very high critical resolved shear stress due to their large magnitudes of Burgers vectors. Therefore the hcp/fcc interface serves as a blocking site for dislocations to cross the phase boundaries. Topologically closely mixing stiff hcp nanolayers with the more pliable and formable fcc nanolayers creates heterogeneous gradient layer substructures at the sheet surface, which increase the material's work hardenability [29,59]. The exceptional strain hardening of the NiCrCo nanolaminate is attributed to the exceptional dislocation storage ability at the nanolaminate interface, as well as the enhanced dislocation interplay with the twin boundaries, stacking faults, and hcp phases [48].

It is worth mentioning that the high internal back stress generated from the heterogeneous grain structure (HGS) also plays an important role in strain hardening. Yang et al. studied the tension behavior of HGS MEA with grain sizes spanning from nanometers to microns and found that strain hardening experienced an upturn during the transient stage of straining. The internal back stress measured can reach ~ 800 MPa [45]. In our work, a very

sluggish decrease in the strain hardening rate is observed within the 200–600 MPa range of ($\sigma_f - \sigma_{0.2}$) for gradient nanolaminate NiCrCo MEA, manifesting the influence of back stress hardening. Upon straining, the soft micron-sized grains yield in advance, and the dislocations generated are blocked by elastic small grains. An excess of geometrically necessary dislocations (GNDs) is generated to accommodate the strain gradients, leading to long-range back stress hardening.

4.3. Phase stability of hcp nanostructures

In the previous section, we stated that having hcp plates is beneficial to additional strain hardening in the gradient MEA nanolaminate. The experimental results presented in Figs. 1 and 2 show a temperature-dependent phase transformation for MEA nanolaminates, where nanoscaled hcp structures are observed at the twin boundaries (i.e., ... CBACB (AB)ⁿABC ...) and also inside the fcc matrix (i.e., ... ABC(AB)ⁿABC ...) after cryogenic hard turning. *Ab-initio* calculations have been used to simulate the relative

thermodynamic stability of the fcc and hcp structures. Rather than treating the nanostructured hcp phase as a bulk state such as shown in previous studies [47], the actual size of the hcp phase (the number of the closest-packed atomic layers, n) was considered as a variable in the free energy calculations. According to the axial next nearest neighbor Ising (ANNNI) model [60], the energies of any nanostructures consisting of A, B, and C planes can be expressed by the energies of simple crystal structures. More specifically, within the ANNNI model the energies of the nanostructures, F , can be expanded into a theoretically infinite series:

$$F = - \sum_{n=0}^2 \sum_i J_n S_i S_{i+n}; \quad (7)$$

assuming that the atomic layers i and $i+n$, characterized by the corresponding spin-numbers S_i and S_{i+n} , interact via interaction parameters J_n . The first two interaction parameters are expressed by Ref. [55].

$$J_1 = \frac{1}{2} (F_{hcp} - F_{fcc}), \quad J_2 = \frac{1}{2} (F_{dhcp} - F_{fcc} - J_1); \quad (8)$$

where F_{fcc} , F_{hcp} and F_{dhcp} are the free energies (normalized to the number of layers) of the fcc (ABCABC stacking), hcp (ABAB stacking), and double-hcp (ABACABAC stacking) phases. Focusing on the hcp nanostructures with a layer thickness of n , the corresponding excess energy over that of the perfect fcc nanocrystal, ΔF , gives.

(i). hcp laths located at fcc twin boundary (TB):

$$\Delta F \approx (4n + 2)J_1 + 4J_2 = 2(F_{dhcp} - F_{fcc}) + 2n(F_{hcp} - F_{fcc}); \quad (9)$$

(ii). hcp laths located in fcc matrix:

$$\Delta F \approx 4nJ_1 + 4J_2 = 2(F_{dhcp} - F_{fcc}) + (2n - 1)(F_{hcp} - F_{fcc}); \quad (10)$$

The free energies of fcc (F_{fcc}), hcp (F_{hcp}), and dhcp (F_{dhcp}) per atom can be determined by the thermodynamic model presented in our methodology section. The solutions of $\Delta F = 0$ give the transition temperatures between the fcc stacking and the hcp nanostructures with a certain layer thickness (n).

Fig. 9 shows the calculated transition temperatures between the fcc stacking and the hcp nanostructure. The black line (394 K) marks the transition temperature between fcc and hcp as bulk phases. Hcp is thermodynamically stable at low temperatures (green area) and fcc is the high temperature-stable phase (orange area). By considering the sizes and nucleation positions of the hcp nanostructures, the exact transition temperatures are calculated by the free energy difference between hcp nanostructure and fcc phase. The theory shows that the formation of lath hcp layers instead of a pure bulk fcc phase at a fixed low temperature is more energetically favorable. Although the exact transition temperature shown here may provide only a qualitative range, as external boundary conditions such as the applied stress are not considered, the calculations provide guidance to better understand why we observe only very thin hcp laths instead of bulk phases in Fig. 1.

5. Conclusions and outlook

In this study, we processed a NiCoCr MEA by hard turning at RT and cryogenic temperatures. Probing with APT and TEM, in tandem with nanomechanical experiments, revealed that atomic-scale

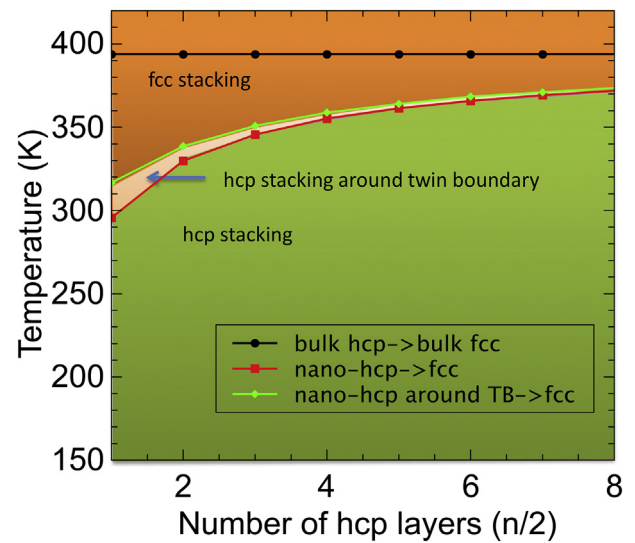


Fig. 9. Relative thermodynamic stability of nanostructures calculated by joint density functional theory (DFT) and axial next nearest neighbor Ising (ANNNI) simulations. DFT computed transition temperatures between experimentally observed nanostructured hcp laths at twin boundaries and in fcc matrix. The transition temperatures were calculated at different numbers of hcp layers (n) following the ANNNI model (see equations (1) and (2)). The hcp layers located in the fcc matrix (red line) and that at fcc twin boundaries (green line) have similar yet different transition temperatures. The black line is the bulk hcp to fcc transition temperature and is shown here for reference. (For interpretation of the references to color in this figure legend, the reader is referred to the Web version of this article.)

hierarchically structured nanolaminate gradients formed at the alloy surface. The layered structure can be manipulated by the shear strain rate and the thermal conditions, parameters that can be directly controlled by adjusting the processing parameters such as turning rate and temperature. The hard turning process introduces complex nanostructures that are characterized not only by nanotwins and nanoscale hcp transformation zones but also by through-thickness gradients of these features. This nanoscale surface hierarchy combines the advantages of stiff hcp regions, a compliant fcc matrix, and a high density of internal interfaces, which leads to high yield stress and high strain hardening during the deformation. In view of these excellent properties, we suggest that this simple and efficient processing technique has wide potential for the high-throughput nanostructural design of alloys with TRIP and TWIP mechanisms, which are also amenable to commercial and large-scale manufacturing.

Acknowledgments

The authors are grateful for the discussion with Dr. Vikram Bedekar, Robert A. Pendergrass, and Andrew A. Markja at the Timken Company. This research was supported primarily by the U.S. Department of Energy, Office of Science, Basic Energy Sciences, Materials Sciences and Engineering Division. Electron microscopy and atom probe tomography experiments were conducted at ORNL's Center for Nanophase Materials Sciences (CNMS), which is a U.S. Department of Energy Office of Science User Facility.

Appendix A. Supplementary data

Supplementary data to this article can be found online at <https://doi.org/10.1016/j.actamat.2019.03.024>.

References

- [1] T.H. Fang, W.L. Li, N.R. Tao, K. Lu, Revealing extraordinary intrinsic tensile plasticity in gradient nano-grained copper, *Science* 331 (6024) (2011) 1587–1590.
- [2] F. Nogata, H. Takahashi, Intelligent functionally graded material - bamboo, *Compos. Eng.* 5 (7) (1995) 743–751.
- [3] A. Miserez, T. Schneberk, C.J. Sun, F.W. Zok, J.H. Waite, The transition from stiff to compliant materials in squid beaks, *Science* 319 (5871) (2008) 1816–1819.
- [4] A. Di Luca, A. Longoni, G. Criscenti, C. Mota, C. van Blitterswijk, L. Moroni, Toward mimicking the bone structure: design of novel hierarchical scaffolds with a tailored radial porosity gradient, *Biofabrication* 8 (4) (2016).
- [5] D. Raabe, P. Romano, C. Sachs, H. Fabritius, A. Al-Sawalmih, S.B. Yi, G. Servos, H.G. Hartwig, Microstructure and crystallographic texture of the chitin–protein network in the biological composite material of the exoskeleton of the lobster *Homarus americanus*, *Mater. Sci. Eng., A* 421 (1–2) (2006) 143–153.
- [6] S.E. Naleway, M.M. Porter, J. McKittrick, M.A. Meyers, Structural design elements in biological materials: application to bioinspiration, *Adv. Mater.* 27 (37) (2015) 5455–5476.
- [7] S.Q. Deng, A. Godfrey, W. Liu, N. Hansen, A gradient nanostructure generated in pure copper by platen friction sliding deformation, *Scripta Mater.* 117 (2016) 41–45.
- [8] J. Sun, Y. Ding, N.J. Lin, J. Zhou, H. Ro, C.L. Soles, M.T. Cicerone, S. Lin-Gibson, Exploring cellular contact guidance using gradient nanogratings, *Biomacromolecules* 11 (11) (2010) 3067–3072.
- [9] P.R. Cantwell, M. Tang, S.J. Dillon, J. Luo, G.S. Rohrer, M.P. Harmer, Grain boundary complexions, *Acta Mater.* 62 (2014) 1–48.
- [10] H. Cao, J.O. Tegenfeldt, R.H. Austin, S.Y. Chou, Gradient nanostructures for interfacing microfluidics and nanofluidics, *Appl. Phys. Lett.* 81 (16) (2002) 3058–3060.
- [11] E. Ma, T. Zhu, Towards strength–ductility synergy through the design of heterogeneous nanostructures in metals, *Mater. Today* 20 (6) (2017) 323–331.
- [12] X. Wu, M. Yang, F. Yuan, G. Wu, Y. Wei, X. Huang, Y. Zhu, Heterogeneous lamella structure unites ultrafine-grain strength with coarse-grain ductility, *Proc. Natl. Acad. Sci. U. S. A.* 112 (47) (2015) 14501–14505.
- [13] X. Wu, P. Jiang, L. Chen, F. Yuan, Y.T. Zhu, Extraordinary strain hardening by gradient structure, *Proc. Natl. Acad. Sci. U. S. A.* 111 (20) (2014) 7197–7201.
- [14] X.L. Wu, M.X. Yang, F.P. Yuan, L. Chen, Y.T. Zhu, Combining gradient structure and TRIP effect to produce austenite stainless steel with high strength and ductility, *Acta Mater.* 112 (2016) 337–346.
- [15] C.W. Shao, P. Zhang, Y.K. Zhu, Z.J. Zhang, Y.Z. Tian, Z.F. Zhang, Simultaneous improvement of strength and plasticity: additional work-hardening from gradient microstructure, *Acta Mater.* 145 (2018) 413–428.
- [16] X.C. Liu, H.W. Zhang, K. Lu, Strain-induced ultrahard and ultrastable nanolaminated structure in nickel, *Science* 342 (6156) (2013) 337–340.
- [17] L. Yang, N.R. Tao, K. Lu, L. Lu, Enhanced fatigue resistance of Cu with a gradient nanograin surface layer, *Scripta Mater.* 68 (10) (2013) 801–804.
- [18] S.D. Lu, Z.B. Wang, K. Lu, Enhanced chromizing kinetics of tool steel by means of surface mechanical attrition treatment, *Mater. Sci. Eng., A* 527 (4–5) (2010) 995–1002.
- [19] X.L. Ma, C.X. Huang, W.Z. Xu, H. Zhou, X.L. Wu, Y.T. Zhu, Strain hardening and ductility in a coarse-grain/nanostructure laminate material, *Scripta Mater.* 103 (2015) 57–60.
- [20] Z. Zurecki, R. Ghosh, J.H. Frey, Investigation of White Layers Formed in Conventional and Cryogenic Hard Turning of Steels, 2003, pp. 211–220, 37203.
- [21] V. Bedekar, R. Shivpuri, A. Avishai, R.S. Hyde, Transmission Kikuchi Diffraction study of texture and orientation development in nanostructured hard turning layers, *CIRP Ann. - Manuf. Technol.* 64 (1) (2015) 73–76.
- [22] V. Bedekar, J.D. Poplawsky, W. Guo, R. Shivpuri, R. Scott Hyde, Atomic migration of carbon in hard turned layers of carburized bearing steel, *CIRP Ann. - Manuf. Technol.* 65 (1) (2016) 85–88.
- [23] B. Gludovatz, A. Hohenwarter, K.V. Thurston, H. Bei, Z. Wu, E.P. George, R.O. Ritchie, Exceptional damage-tolerance of a medium-entropy alloy CrCoNi at cryogenic temperatures, *Nat. Commun.* 7 (2016) 10602.
- [24] Z. Wu, H. Bei, G.M. Pharr, E.P. George, Temperature dependence of the mechanical properties of equiatomic solid solution alloys with face-centered cubic crystal structures, *Acta Mater.* 81 (2014) 428–441.
- [25] S. Zhao, G.M. Stocks, Y. Zhang, Stacking fault energies of face-centered cubic concentrated solid solution alloys, *Acta Mater.* 134 (2017) 334–345.
- [26] W. Guo, D. Garfinkel, A.J. Tucker, D.D. Haley, G. Young, A.J. Poplawsky D, An atom probe perspective on phase separation and precipitation in duplex stainless steels, *Nanotechnology* 27 (25) (2016) 254004.
- [27] K. Thompson, D. Lawrence, D.J. Larson, J.D. Olson, T.F. Kelly, B. Gorman, In situ site-specific specimen preparation for atom probe tomography, *Ultramicroscopy* 107 (2–3) (2007) 131–139.
- [28] W.C. Oliver, G.M. Pharr, An improved technique for determining hardness and elastic-modulus using load and displacement sensing indentation experiments, *J. Mater. Res.* 7 (6) (1992) 1564–1583.
- [29] W. Guo, E. Jagle, J.H. Yao, V. Maier, S. Korte-Kerzel, J.M. Schneider, D. Raabe, Intrinsic and extrinsic size effects in the deformation of amorphous CuZr/nanocrystalline Cu nanolaminates, *Acta Mater.* 80 (2014) 94–106.
- [30] D.C. Ma, B. Grabowski, F. Kormann, J. Neugebauer, D. Raabe, Ab initio thermodynamics of the CoCrFeMnNi high entropy alloy: importance of entropy contributions beyond the configurational one, *Acta Mater.* 100 (2015) 90–97.
- [31] S.J. Zhao, G.M. Stocks, Y.W. Zhang, Stacking fault energies of face-centered cubic concentrated solid solution alloys, *Acta Mater.* 134 (2017) 334–345.
- [32] Z. Zhang, H. Sheng, Z. Wang, B. Gludovatz, Z. Zhang, E.P. George, Q. Yu, S.X. Mao, R.O. Ritchie, Dislocation mechanisms and 3D twin architectures generate exceptional strength–ductility–toughness combination in CrCoNi medium-entropy alloy, *Nat. Commun.* 8 (2017) 14390.
- [33] B. Grabowski, P. Soderlind, T. Hickel, J. Neugebauer, Temperature-driven phase transitions from first principles including all relevant excitations: the fcc-to-bcc transition in Ca, *Phys. Rev. B* 84 (21) (2011).
- [34] V.L. Moruzzi, J.F. Janak, K. Schwarz, Calculated thermal properties of metals, *Phys. Rev. B Condens. Matter* 37 (2) (1988) 790–799.
- [35] G. Kresse, D. Joubert, From ultrasoft pseudopotentials to the projector augmented-wave method, *Phys. Rev. B* 59 (3) (1999) 1758–1775.
- [36] G. Kresse, J. Furthmüller, Efficient iterative schemes for ab initio total-energy calculations using a plane-wave basis set, *Phys. Rev. B* 54 (16) (1996) 11169–11186.
- [37] J.P. Perdew, K. Burke, M. Ernzerhof, Generalized gradient approximation made simple, *Phys. Rev. Lett.* 77 (18) (1996) 3865–3868.
- [38] K. Lu, L. Lu, S. Suresh, Strengthening materials by engineering coherent internal boundaries at the nanoscale, *Science* 324 (5925) (2009) 349–352.
- [39] Z.H. Jin, P. Gumbsch, K. Albe, E. Ma, K. Lu, H. Gleiter, H. Hahn, Interactions between non-screw lattice dislocations and coherent twin boundaries in face-centered cubic metals, *Acta Mater.* 56 (5) (2008) 1126–1135.
- [40] M. Herbig, M. Kuzmina, C. Haase, R.K.W. Marceau, I. Gutierrez-Urrutia, D. Haley, D.A. Molodov, P. Choi, D. Raabe, Grain boundary segregation in Fe–Mn–C twinning-induced plasticity steels studied by correlative electron backscatter diffraction and atom probe tomography, *Acta Mater.* 83 (2015) 37–47.
- [41] K.E. Spear, J.P. Dismukes, S. Electrochemical, *Synthetic Diamond : Emerging CVD Science and Technology*, Wiley, New York, 1994.
- [42] T.-Y. Kim, J.E. Dolbow, E. Fried, Numerical study of the grain-size dependent Young's modulus and Poisson's ratio of bulk nanocrystalline materials, *Int. J. Solids Struct.* 49 (26) (2012) 3942–3952.
- [43] X. Chen, Z. Han, X. Li, K. Lu, Lowering coefficient of friction in Cu alloys with stable gradient nanostructures, *Science Advances* 2 (12) (2016) e1601942.
- [44] P.F. Wang, Z. Han, K. Lu, Enhanced tribological performance of a gradient nanostructured interstitial-free steel, *Wear* 402–403 (2018) 100–108.
- [45] M. Yang, D. Yan, F. Yuan, P. Jiang, E. Ma, X. Wu, Dynamically reinforced heterogeneous grain structure prolongs ductility in a medium-entropy alloy with gigapascal yield strength, *Proc. Natl. Acad. Sci. Unit. States Am.* 115 (28) (2018) 7224–7229.
- [46] G. Laplanche, A. Kostka, O.M. Horst, G. Eggeler, E.P. George, Microstructure evolution and critical stress for twinning in the CrMnFeCoNi high-entropy alloy, *Acta Mater.* 118 (2016) 152–163.
- [47] J. Miao, C.E. Slone, T.M. Smith, C. Niu, H. Bei, M. Ghazisaeidi, G.M. Pharr, M.J. Mills, The evolution of the deformation substructure in a Ni–Co–Cr equiatomic solid solution alloy, *Acta Mater.* 132 (2017) 35–48.
- [48] Y. Ma, F. Yuan, M. Yang, P. Jiang, E. Ma, X. Wu, Dynamic shear deformation of a CrCoNi medium-entropy alloy with heterogeneous grain structures, *Acta Mater.* 148 (2018) 407–418.
- [49] Y. Peng, J. Chu, J. Dong, Compressive behavior and constitutive model of austenitic stainless steel S30403 in high strain range, *Materials* 11 (6) (2018).
- [50] N.K.S. Ajay K. Behera, Maloy K. Singha, Compressive behavior of AISI-416 stainless steel at different rates of loading, in: *Proceedings of the World Congress on Engineering 2012*, London, U.K., 2012, pp. 1879–1883.
- [51] G. Laplanche, A. Kostka, C. Reinhart, J. Hunfeld, G. Eggeler, E.P. George, Reasons for the superior mechanical properties of medium-entropy CrCoNi compared to high-entropy CrMnFeCoNi, *Acta Mater.* 128 (2017) 292–303.
- [52] L. Lu, Z.S. You, K. Lu, Work hardening of polycrystalline Cu with nanoscale twins, *Scripta Mater.* 66 (11) (2012) 837–842.
- [53] Z. Li, K.G. Pradeep, Y. Deng, D. Raabe, C.C. Tasan, Metastable high-entropy dual-phase alloys overcome the strength–ductility trade-off, *Nature* 534 (7606) (2016) 227–230.
- [54] J. Moon, Y. Qi, E. Tabachnikova, Y. Estrin, W.-M. Choi, S.-H. Joo, B.-J. Lee, A. Podolskiy, M. Tikhonovskiy, H.S. Kim, Deformation-induced phase transformation of Co 20 Cr 26 Fe 20 Mn 20 Ni 14 high-entropy alloy during high-pressure torsion at 77 K, *Mater. Lett.* 202 (2017) 86–88.
- [55] S. Sandlobes, M. Friak, S. Zaefferer, A. Dick, S. Yi, D. Letzig, Z. Pei, L.F. Zhu, J. Neugebauer, D. Raabe, The relation between ductility and stacking fault energies in Mg and Mg–Y alloys, *Acta Mater.* 60 (6–7) (2012) 3011–3021.
- [56] S. Sandlobes, M. Friak, S. Korte-Kerzel, Z. Pei, J. Neugebauer, D. Raabe, A rare-earth free magnesium alloy with improved intrinsic ductility, *Sci. Rep.* 7 (2017).
- [57] A. Takeuchi, K. Amiya, T. Wada, K. Yubuta, W. Zhang, High-entropy alloys with a hexagonal close-packed structure designed by equi-atomic alloy strategy and binary phase diagrams, *JOM (J. Occup. Med.)* 66 (10) (2014) 1984–1992.
- [58] K.M. Youssef, A.J. Zaddach, C. Niu, D.L. Irving, C.C. Koch, A novel low-density, high-hardness, high-entropy alloy with close-packed single-phase nanocrystalline structures, *Materials Research Letters* 3 (2) (2014) 95–99.
- [59] Y.M. Wang, J. Li, A.V. Hamza, T.W. Barbee, Ductile crystalline-amorphous nanolaminates, *P Natl Acad Sci USA* 104 (27) (2007) 11155–11160.
- [60] P.J.H. Denteneer, W.v. Haeringen, Stacking-fault energies in semiconductors from first-principles calculations, *J. Phys. C Solid State Phys.* 20 (32) (1987) L883.